Definition of vortex boundary using stagnation pressure

Marc Plasseraud● and Krishnan Mahesh[*]

Naval Architecture & Marine Engineering, University of Michigan, Ann Arbor, 48109, Michigan, USA

A method is proposed to identify the vortex boundary and center of rotation based on tubular surfaces of constant stagnation pressure and minimum of the stagnation pressure gradient. The method is derived from Crocco's theorem, which ensures that the gradient of stagnation pressure is orthogonal to both the velocity and vorticity vectors. The method is Galilean invariant, requires little processing, and is robust. It enables visualization of complex turbulent flows and provides a physically consistent definition of vortex boundaries for quantitative analyses. This vortex boundary is a material surface that is representative of the kinematics of the flow by construction, constitutes a vortex tube, ensures the conservation of circulation in the inviscid limit, and provides a unique relation to the conservation of momentum equations and vortex loads.

I. INTRODUCTION

Vortices are a near-universal and characteristic feature of fluid flows. Defining their boundary and centerline is crucial for understanding flow behavior, loads and, more fundamentally, energy transport in turbulence. While they are easy to identify visually, there is no consensus on the mathematical definition of what constitutes a vortex, and what Lugt [1] aptly called the "dilemma of defining a vortex" is still a topic of active research. Robinson [2] groups vortices into a more general category of coherent motions, which is the foundation of turbulent structures. This definition perhaps hints at the difficulty encountered in trying to use a metric that is local and instantaneous to describe a phenomenon that is fundamentally nonlocal (spatial coherence) and transient (temporal coherence) while being usable across a wide variety of flows. Several methods have been proposed and successfully applied [3,4]. The difficulty generally resides in finding an objective metric [5] that can accommodate a large variety of vortex types while distinguishing between shearing and vortical vorticity. In their review of vortex identification, Epps [4] formalizes a list of requirements for methods, which includes among others: be objective; avoid the use of an arbitrary threshold; identify coherent motion; guarantee nonzero vorticity; be insensitive to shear vorticity; be applicable to compressible flows and heterogeneous fluids; and be robust to experimental noise. In addition to these criteria, secondary properties are desirable: a method should be computationally inexpensive and favor the use of local variables, and not depend on higher order quantities that can be slow to converge and thus require long sampling times. Many methods exist that have verified some part of these requirements [3,4] although none validate all of them. Some of the most commonly used methods include the following:

(1) Pressure [2]: vortices can be identified as minima of pressure. This method has the advantage of simplicity and being invariant, however, the presence of a minimum of pressure does not guarantee the existence of a vortex. Worse, the presence of a vortex does not guarantee a minimum of pressure such as in the case of vortices with strong axial velocity (see Sec. V). Instead of using pressure directly, Li and Carrica [6] used the gradient of pressure normalized by its Laplacian

---

[*]Contact author: krmahesh@umich.edu

114701-1

as a distance field to the vortex core. This approach recovers the radius of a Rankine vortex and shows promising results for the cases demonstrated in their study such as homogeneous isotropic turbulence however, as the authors note, it is limited to cases where the pressure gradient originates from the vortex.

(2) Vorticity magnitude or axial vorticity [7]: Saffman [7] defines vortices as a connected region of vorticity. In accordance with this definition, vortices can be identified through a maximum of axial vorticity although this requires *a priori* knowledge of the axis of vorticity; or through the maximum of enstrophy [8]. This method is simple and the presence of a vortex guarantees the existence of a local extrema of vorticity, however, it does not distinguish between shear layer and vortices.

(3) The Q criterion method, proposed by Hunt *et al.* [9] and refined by Dubief and Delcayre [10] using a Large Eddy Simulation and direct numerical simulation, identifies vortices as regions where the Q value is positive with

$$Q = ||\Omega||_2^2 - ||S||_2^2,$$

where S is the strain rate tensor and Ω is the rotation tensor. Positive values are indicative of regions with strong streamline curvature.

(4) Jeong and Hussain [11] proposed another velocity gradient tensor-based method based on the second eigenvalue of the matrix $\Omega^2 + S^2$. It uses the fact that a negative second eigenvalue is indicative of a rotation-dominated area of the flow, to identify coherent rotating motion. Both the Q criterion and λ_2 methods are widely used and identify vortices in strong vorticity regions and discriminate efficiently between shear layer and coherent motion, however, they can generate false positives (corner flow for example) and may not align as well with more intuitive streamlined definitions (see Sec. IV). Their limitation comes from the exclusive use of kinematic variables, and it will be shown that they fail in the case of a cavity flow where the streamlines are curved outside a vortex. In addition, although both Q and λ_2 are Galilean invariant; they are not objective.

(5) Lagrangian based [12]: these methods define vortices in terms of particle trajectory such as closed streamlines. While they give results that are close to the qualitative observation of vortices, they are harder to use since they rely on nonlocal and time-varying variables. In addition, it can be difficult to assess whether streamlines are closed, especially for three-dimensional vortices. Furthermore, using velocity vectors is not an objective metric. It may give a different result if a constant velocity component is added to the field [1]. Haller *et al.* [13] and Neamtu-Halic *et al.* [14] proposed the Lagrangian-averaged vorticity deviation (LAVD) and instantaneous vorticity deviation (IVD), both of which use the vorticity field to deduce the Lagrangian Coherent Structures as an indication of vortices.

Despite the multitude of methods available, none offers both a robust way of visualizing vortices in complex flow and a way to identify vortex topology in accordance with the kinematics of the flow and conservation laws. Vorticity-based and Lagrangian methods are impractical for the former while the Q criterion and λ_2 are unreliable for the latter. The goal of this study is to propose a vortex identification method that can visualize complex turbulent flows while providing individual vortex boundaries and centers that are physically sound. The latter is required so that vortex properties such as loads, circulation, and flux can be measured in a way that is flow agnostic. The process should not rely on complex calculations and should only use variables that are readily available. The proposed alternative shows similar results to the state-of-the-art λ_2 method for visualizing tripped boundary layer flow and flow over a cylinder while it outperforms it on a lid-driven cavity flow and the flow over a 6:1 prolate spheroid at angle of attack. It is simple, fast to converge, and gives a general definition for purpose of quantitative vortex analyses.

II. THEORETICAL BASIS

The momentum equation is written in a translating reference frame following a vortex. Let $\vec{u} = u_i$, $P = P'/\rho$, and $\bar{\bar{\tau}} = \tau_{ij}$ be the instantaneous velocity relative to the center of the vortex, pressure, density, and specific shear stress. The incompressible momentum equation can be written in index
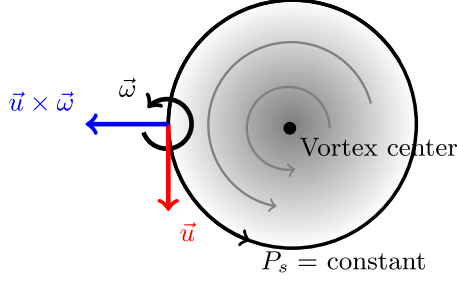
FIG. 1. Schematic of Crocco's theorem applied to a vortex.

notation where a repeated index is used to represent the summation:

$$\frac{\partial u_i}{\partial t} + u_j \frac{\partial u_i}{\partial x_j} = -\frac{\partial P}{\partial x_i} + \frac{1}{\rho} \frac{\partial \tau_{ij}}{\partial x_j}. \tag{1}$$

The convection term can be written as

$$u_j \frac{\partial u_i}{\partial x_j} = \frac{1}{2} \frac{\partial u_j u_j}{\partial x_i} - u_j \omega_k \epsilon_{ijk} e_i,$$

where e_i is the unit vector along the ith coordinate and ϵ_{ijk} is the Levi-Civita symbol. This expression is inserted into Eq. (1). In addition, it is assumed that the mean flow velocity in the vortex is constant thus $\partial u_i / \partial t = U_j \partial u_i / \partial x_j = 0$ with the mean flow velocity $U_j = 0$ since the chosen reference frame follows a vortex

$$\frac{1}{2} \frac{\partial u_j u_j}{\partial x_i} - u_j \omega_k \epsilon_{ijk} e_i = -\frac{\partial P}{\partial x_i} + \frac{\partial \tau_{ij}}{\partial x_j},$$

$$u_j \omega_k \epsilon_{ijk} e_i = \frac{\partial}{\partial x_i}\left(P + \frac{1}{2} u_i u_i\right) - \frac{\partial \tau_{ij}}{\partial x_j}.$$

The stagnation pressure is written as $P_s = P + \frac{1}{2} u_i u_i$, yielding

$$u_j \omega_k \epsilon_{ijk} e_i = \frac{\partial P_s}{\partial x_i} - \frac{\partial \tau_{ij}}{\partial x_j}.$$

This yields Crocco's theorem for viscous flows in vector notation:

$$\vec{u} \times \vec{\omega} = \nabla P_s + \nabla \cdot \tau. \tag{2a}$$

$\vec{u} \times \vec{\omega}$ is referred to as the Lamb vector where $\times$ is the cross product. If the Reynolds number is sufficiently high, the viscous term is negligible and the equation becomes

$$\vec{u} \times \vec{\omega} \approx \nabla P_s. \tag{2b}$$

Note that Eq. (2b) is instantaneous and allows visualization of turbulent flows assuming steady flow inside the eddies in accordance with Taylor's hypothesis. This hypothesis may not be valid for certain flows, for example, large coherent recirculation vortices. In this case, a time-averaged variant can be used:

$$\langle \vec{u} \times \vec{\omega} \rangle \approx \nabla \langle P_s \rangle, \tag{2c}$$

where the bracket $\langle \cdot \rangle$ indicates time averaging.

Figure 1 illustrates the terms of Eq. (2b). The velocity vector follows the streamline by definition and ∇P_s is orthogonal to the streamline since $\vec{u} \times \vec{\omega} = \nabla P_s$. This means that streamlines are tangential to the isosurfaces of P_s. Since $\vec{u} \times \vec{\omega}$ is also orthogonal to $\vec{\omega}$, the vorticity vectors are
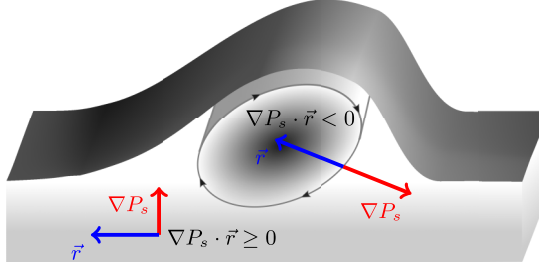
FIG. 2. Schematic illustrating the $\nabla P_s \cdot \vec{r}$ condition for a vortex in a shear layer.

also tangential to the isosurfaces of P_s. This result is discussed by Truesdell [15] in restrictive complex-lamellar cases where $\vec{u} \cdot \vec{\omega} = 0$ and $\|\vec{\omega}\| = 0$. The $\vec{u} \times \vec{\omega}$ isosurfaces are referred to as Lamb surfaces. These surfaces have the interesting property of containing both the streamlines and the vortex lines. An intuitive way of defining a vortex is to consider the interior of closed streamlines, however, it is difficult to assess whether streamlines are closed in practice. They also depend on the coordinate frame and may not close at all if the vortex is three-dimensional. This issue can be resolved by observing that a closed streamline will be contained inside a tube of constant stagnation pressure since the streamlines are tangential to the Lamb surfaces. Thus a way to define a vortex is to consider a closed Lamb surface, which has several advantages over more commonly used vortex identification methods:

(1) The Lamb tube is a material boundary in a steady flow [15] which ensures conservation of circulation along its axis. Since the steady Lamb tube is material, it is also objective.

(2) Because the streamlines are tangent to the Lamb surfaces, the boundary of the vortex is consistent with a Lagrangian definition while relying on Eulerian metrics, which are simpler to evaluate.

(3) The net flux of momentum and vorticity across the boundary is zero, hence the loads integrated over the volume of a vortex core is zero. The loads of the vortex over a nearby wall originate from the intersection of Lamb surfaces and the wall.

Note that these properties of the Lamb surface assume a non-Beltrami flow. In addition, the inviscid and incompressible assumptions are necessary to equate the Lamb vector to the gradient of stagnation pressure.

The right-hand side of Eq. (2c) can be expanded using a Reynolds decomposition where u'_i is the velocity perturbation:

$$\nabla \langle P_s \rangle = \nabla (\langle P \rangle + \tfrac{1}{2} \langle u_i \rangle \langle u_i \rangle + \tfrac{1}{2} \langle u'_i u'_i \rangle).$$

This form shows that Eq. (2c) applied to a vortex is a statement of energy conservation, stored in the form of potential energy P, mean kinetic energy $\tfrac{1}{2} \langle u_i \rangle \langle u_i \rangle$, and turbulent kinetic energy $\tfrac{1}{2} \langle u'_i u'_i \rangle$. Consider the curvature vector $\vec{r}$ (which can be obtained by normalization of $\partial \vec{u} / \partial s = \partial u_i / \partial x_j \cdot u_j / \|\vec{u}\|$, where s is the streamwise coordinate), pointing from in the direction of the vortex center thus colinear with ∇P_s. Moving in the direction of $\vec{r}$ from the periphery to the center, the total energy decreases as the enclosed region contains less integrated vorticity thus $\nabla P_s \cdot \vec{r} < 0$. This is illustrated in Fig. 2, showing that within the vortex, the gradient is not only aligned with the direction of curvature but P_s also decreases toward the center. Outside the vortex, however, P_s either decreases outward or is constant with the radius. $\vec{r}$, on the other hand, always points toward the center of rotation by definition. Thus the sign of $\nabla P_s \cdot \vec{r}$ can inform the region dominated by the vortex. The following vortex definition is proposed:

(1) Vortex as a region enclosed by a Lamb surface.

(2) Vortex boundary may locally be retrieved as $(\vec{u} \times \vec{\omega}) \cdot \vec{r} < 0$, $\vec{r}$ can be calculated by normalization of the vector $\partial u_i / \partial x_j \cdot u_j$.

These two criteria are objective metrics that are subject to the assumption of a non-Beltrami flow. Under the previously discussed assumptions, Eqs. (2b) and (2c) may instead be used to relax the vortex definition as:

(1) Vortex region: $P_s \leqslant P_s^0$ where P_s^0 is a closed isosurface.

(2) The vortex boundary may alternatively be retrieved locally as: $\nabla P_s \cdot \vec{r} < 0$, with $\|\nabla P_s\| \neq 0$. $\vec{r}$ can be calculated by normalization of the vector $\partial u_i / \partial x_j \cdot u_j$.

The first condition ensures that the vortex boundary is a material surface, more specifically a vortex tube that conserves circulation along its axis and has zero momentum deficit hence zero load. The second condition identifies regions where the Lamb vector is aligned with the local streamline curvature. Note that the first statement (closed isosurface) does not rely on an arbitrary threshold and may be evaluated using a flood-fill algorithm. While the theory behind the second criterion ($\nabla P_s \cdot \vec{r} < 0$) does not depend on a threshold, in practice for visualization purposes, small negative values may be necessary to isolate vortices of higher strength. This is similar to commonly used methods such as Q or λ_2, which are usually used with thresholds that are more stringent than zero. The stagnation pressure field also provides another desirable feature of vortex identification methods, which is to locate the center. At a vortex center, the normalized helicity density is maximized [16] thus the normal of the Lamb vector $\|\vec{u} \times \vec{\omega}\|$ is minimized [17]. The center of the vortex can then be found as a local minimum of stagnation pressure and its gradient.

A. Approximation of Lamb surfaces for experimental purposes

The pressure field in the fluid may not be readily experimentally, however, in certain conditions, it is possible to approximate Lamb surfaces with surfaces of constant total kinetic energy $K = \frac{1}{2} u_i u_i$. These isosurfaces will approach Lamb surfaces when $\partial P / \partial x_j \ll K$, which is a similar approximation as the one considered by kinematic methods such as λ_2. In these conditions, vortices can be visualized by $\nabla K \cdot \vec{r} \leqslant 0$ surfaces.

B. Connection with vortex loads

Defining vortices based on isolines offers a unique perspective on the vortex loads since the stagnation pressure appears in the momentum equation. Integrating Eq. (2c) over a control volume V, bounded by a surface S and normal $\vec{n}$ gives

$$\int_V \langle \vec{u} \times \vec{\omega} \rangle dV = \int_S \langle P_s \rangle \vec{n} dS,$$

which can be written as

$$F_\omega = \int_S \langle P_s \rangle \vec{n} dS, \tag{3}$$

where

$$F_\omega = \int_V \langle \vec{u} \times \vec{\omega} \rangle dV, \tag{4}$$

represents the net momentum from vorticity in the control volume [18,7], which equates the divergence of the stagnation pressure. If the boundary of a vortex is defined as a closed isoline of stagnation pressure of constant value P_s^{iso}, the equation becomes

$$F_\omega = \int_S \langle P_s^{\text{iso}} \rangle \vec{n} dS = \langle P_s^{\text{iso}} \rangle \int_S \vec{n} dS = 0.$$

This is consistent with the result that the net momentum from an isolated vortex is zero. If the vortex is near a wall, the loads come from the intersection of the isolines of stagnation pressure and such

wall. Indeed, for that case, Eq. (3) becomes

$$F_\omega = \langle P_s^{\text{iso}} \rangle \int_{S_{\text{fluid}}} \vec{n} \, dS + \int_{S_{\text{wall}}} \langle P_s^{\text{wall}} \rangle \vec{n} \, dS. \qquad (5)$$

Where $S = S_{\text{fluid}} \cup S_{\text{wall}}$, the fluid and wall surfaces of the control volume, respectively. Consider a spanwise vortex above a horizontal wall located at $y = 0$ and apply Eq. (5) in a semi-infinite control volume in x and y. Note that the equations are derived in two dimensions for ease of reading although an extension to three dimensions is trivial:

$$
\begin{aligned}
F_\omega \cdot \vec{n}_y &= \langle P_s^{\text{iso}} \rangle \int_{S_{\text{fluid}}} \vec{n} \cdot \vec{n}_y \, dS + \int_{S_{\text{wall}}} \langle P_s^{\text{wall}} \rangle \, dS \\
&= -P_s^\infty \int_{x_{-\infty}}^{x=+\infty} dx + \int_{S_{\text{wall}}} \langle P_s^{\text{wall}} \rangle \, dx \\
&= \int_{x=-\infty}^{x=+\infty} \left\langle P^{\text{wall}} - \left(P^\infty + \frac{1}{2} U_\infty^2 \right) \right\rangle dx.
\end{aligned}
\qquad (6)
$$

Where $P_{\text{wall}} = P'_{\text{wall}}/\rho$ is the static pressure at the wall, P^∞ and U^∞ are the freestream pressure and velocity, respectively. Equation (6) correctly recovers the expected expression of force. In addition, if the domain is size l_x in the x direction with $l_x \to 0$,

$$
\begin{aligned}
lim_{x \to 0} F_\omega \cdot \vec{n}_y &= \int_{y=0}^{y=+\infty} \left\langle P^{\text{wall}} - \left(P^\infty + \frac{1}{2} U_\infty^2 \right) \right\rangle \\
&= \int_{y=0}^{y=+\infty} \frac{1}{2} U_\infty^2 (c_p - 1),
\end{aligned}
\qquad (7)
$$

where $c_p = 2(\langle P^{\text{wall}} \rangle - P^\infty)/U_\infty^2$ is the wall pressure coefficient. Combining Eqs. (4) and (7) yields

$$\int_{y=0}^{y=+\infty} \langle \vec{u} \times \vec{\omega} \rangle dy = \frac{1}{2} U_\infty^2 (c_p - 1). \qquad (8)$$

Equation (8) can be used to identify the contribution of a specific area of the flow to the wall pressure.

C. Procedure

In summary, the following procedure is used to analyze vortical flows.

Calculate stagnation pressure $P_s = P + \frac{1}{2}\vec{u} \cdot \vec{u}$ for unsteady flows or $\langle P_s \rangle = \langle P \rangle + \frac{1}{2}\langle u_i \rangle \langle u_i \rangle + \frac{1}{2}\langle u_i' u_i' \rangle$ for statistically steady flows. Visualization of this variable yields: regions where the flow is rotational (boundary layers, recirculations ...) with values of P_s that are smaller than the free-stream value; vortex centers as local minima of stagnation pressure; vortex core as a region contained in closed isolines of stagnation pressure; and vortex boundary as the largest closed isoline of stagnation pressure. This boundary can be used for the purpose of integral calculation on the vortex.

This approach is simple and yields reliable results for the analysis of a 2D slice of isolated vortices. The following procedure is followed for the purpose of visualizing 3D isosurface in general turbulent flows:

Calculate the gradient of stagnation pressure as

$$\nabla P_s = \frac{\partial P_s}{\partial x_j} = \frac{\partial P}{\partial x_j} + u_i \frac{\partial u_i}{\partial x_j}.$$

Calculate the vector $\vec{r}$, which points toward the center of rotation of the streamline as

$$\vec{r} = \frac{u_j \frac{\partial u_i}{\partial x_j}}{\sqrt{u_k u_k}}.$$

Calculate $\nabla P_s \cdot \vec{r}$ and visualize its negative isosurfaces.

D. Analytical vortex: Rankine model

The Rankine vortex is a simplified two-dimensional model where the fluid moves in solid body rotation within a radius r_0 and where the flow is potential at a distance greater than r_0:

$$u_r = u_z = 0$$
$$u_\theta = u_0 \frac{r}{r_0}, r \leqslant r_0$$
$$u_\theta = u_0 \frac{r_0}{r}, r \geqslant r_0.$$

The momentum equation in cylindrical coordinate simplifies to

$$\frac{\partial P}{\partial r} = \frac{u_\theta^2}{r}.$$

Thus the r derivative of the stagnation pressure is

$$\frac{\partial P_s}{\partial r} = \frac{\partial P}{\partial r} + u_\theta \frac{\partial u_\theta}{\partial r}$$
$$= \begin{cases} \frac{u_0^2 r}{r_0^2} + \frac{u_0^2 r}{r_0^2} = 2\frac{u_0^2 r}{r_0^2}, r < r_0 \\ \frac{u_0^2 r_0^2}{r^3} - \frac{u_0^2 r_0^2}{r^3} = 0, r > r_0 \end{cases}.$$

If the vortex is taken at the boundary where $\nabla P_s \cdot \vec{r} = 0$, in this special case $\partial P_s/\partial r = 0$, the radius of the vortex is perfectly recovered as r_0, thus the method is consistent for a Rankine vortex. In the next paragraphs, the vortex identification method is tested on several numerical cases.

III. NUMERICAL APPROACH

The incompressible, spatially filtered Navier-Stokes equations are solved in a Large Eddy Simulation formulation:

$$\frac{\partial \overline{u}_i}{\partial t} + \frac{\partial}{\partial x_j}(\overline{u}_i \overline{u}_j) = -\frac{\partial \overline{P}}{\partial x_i} + \nu \frac{\partial^2 \overline{u}_i}{\partial x_j \partial x_j} - \frac{\partial \overline{\tau}_{ij}}{\partial x_j}, \tag{9}$$

$$\frac{\partial \overline{u}_i}{\partial x_i} = 0. \tag{10}$$

The subgrid stress (SGS) $\overline{\tau}_{ij} = \overline{u_i u_j} - \overline{u}_i \overline{u}_j$ is modeled with the dynamic Smagorinsky model [19,20]. A finite volume, second-order centered spatial discretization is used where the filtered velocity components and pressure are stored at the cell centroids while the face-normal velocities are estimated at the face centers. The equations are marched in time with a second-order Crank-Nicolson scheme. A diverse range of complex flows have been studied using the formulation, such as propellers in crashback [21,22] and flow over hulls [23,24]. The kinetic-energy conservation property of the method [25] makes it suitable for a high Reynolds number flow such as the one presented in this paper. Horne and Mahesh [26] extended the method for overlapping (overset) grids and six degrees of freedom. Although all the geometries presented in the current study are static, the overset formulation is used to limit the computational cost while increasing the resolution in regions of high shear.
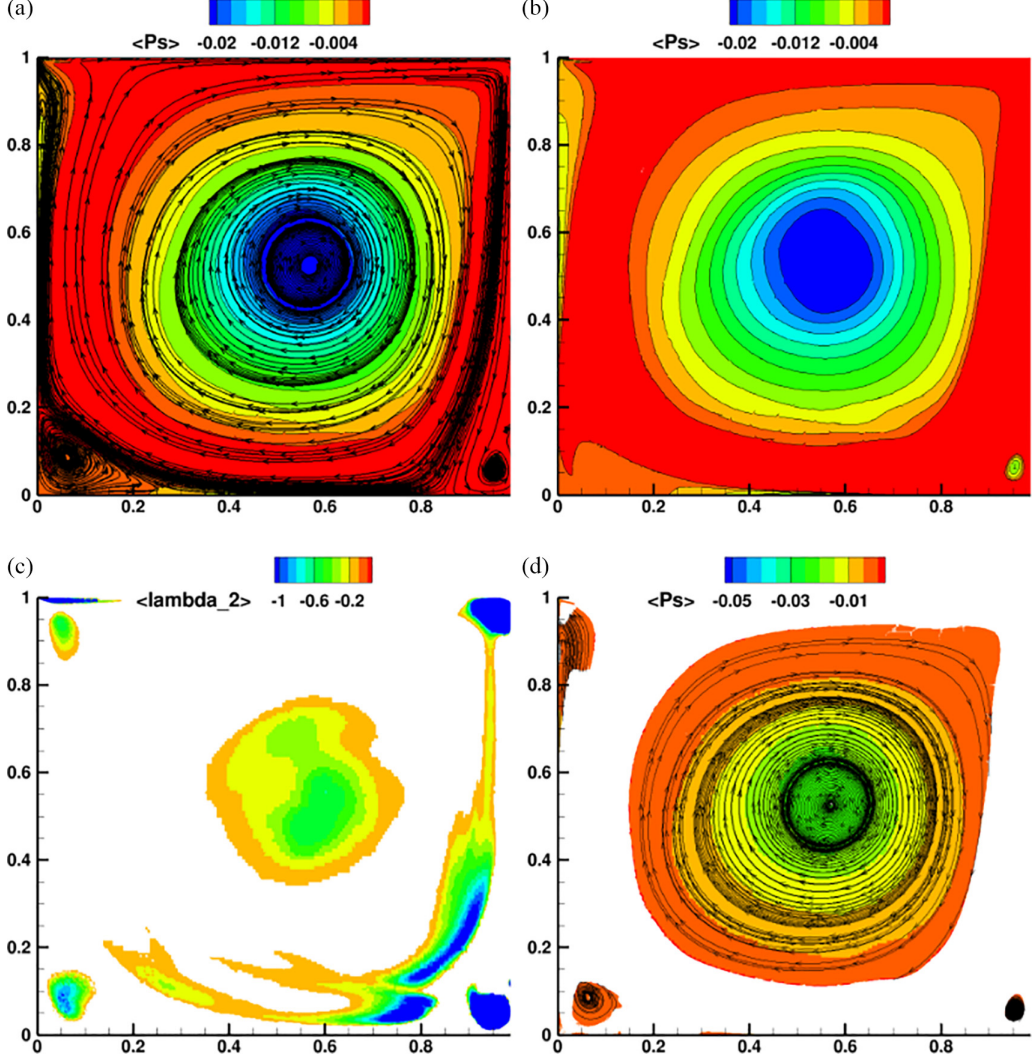
FIG. 3. Averaged velocity streamlines (a) mean stagnation pressure isolines (b) λ_2 masked at $\lambda_2 < -0.1$ (c) and mean stagnation pressure masked by $\nabla P_s \cdot \vec{r} < 0$ (d) in the cavity at $Re = 10\,000$.

IV. CASE I - CAVITY FLOW

A cavity flow is a canonical problem that produces a steady vortex. The chosen Reynolds number is 10 000 for a cubic cavity of unit length in all directions. The top boundary has unit velocity U_0, and no-slip conditions are applied on the bottom and side walls with a periodic boundary on the span. The flow is developed until the loads plateau, which happens at around 40 units. Figure 3 shows the averaged velocity streamlines, the mean stagnation pressure isolines, λ_2 and the mean stagnation pressure blanked by $\nabla P_s \cdot \vec{r}$. Even for this moderate Reynolds number, the isolines of stagnation pressure are very well aligned with the streamlines. The deficit of stagnation pressure correctly identifies the location of the primary vortex and the three secondary vortices. In contrast, λ_2 correctly identifies the primary as well as the secondary vortices, however, the shape of the vortices deviates from the streamlines. In addition, it has several false positives, specifically on the top corner and below the primary vortex. These artifacts occur where the streamlines have significant

TABLE I. Vertical component of the volume integral of the time-averaged Lamb vector and vertical component of the time-averaged forces F_y on the boundary of the cavity.

$\langle \vec{u} \times \vec{\omega} \rangle_y$	F_y top	F_y sides	F_y bottom
0.5071	0.5056	$-4.077e^{-3}$	$-2.064e^{-3}$

curvature, though no vortex is present. The $\nabla P_s \cdot \vec{r}$ criterion correctly identifies all the vortical structures without false positives; the isosurfaces of stagnation pressure are well aligned with the streamlines.As previously mentioned, the method can also be used to estimate loads. Applying Eq. (2a) along the vertical direction and integrating over the cavity yields:

$$\int_V \langle \vec{u} \times \vec{\omega} \rangle \cdot \vec{n}_y dV = - \int_{S_{\text{top}}} \langle P_s \rangle dS + \frac{1}{2} U_0^2 \left(\int_{S_{\text{left}}} c_f dS - \int_{S_{\text{right}}} c_f dS + \int_{S_{\text{bottom}}} c_p dS \right), \qquad (11)$$

where V is the volume of the cavity, $S_{\text{left}}, S_{\text{right}}, S_{\text{bottom}}$ and S_{top} are the surfaces of the back and front walls, c_f is the skin friction coefficient, c_p is the wall pressure coefficient, and P_s is the stagnation pressure.

Table I shows the value of each of the terms of Eq. (11). Even for this moderate Reynolds number, the value of the viscous term is negligible (two orders of magnitude) compared to the pressure terms and the vorticity term. This justifies the inviscid form of Crocco's theorem for vortical flows with a higher Reynolds number based on vortex diameter. This also suggests that the Lamb vector can be used as a way to measure the load contribution of a fluid parcel on the wall. Figure 4 shows its local value, representative of the contribution of the vortical force to the wall: a negative value is indicative of an increased pressure contribution on the bottom wall while a positive value indicates suction. Most of the loads come from the region on the edge of the primary vortex and are suctions,
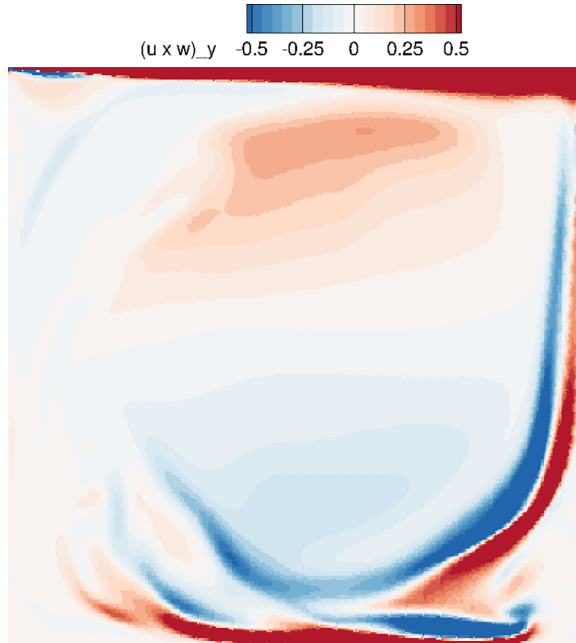
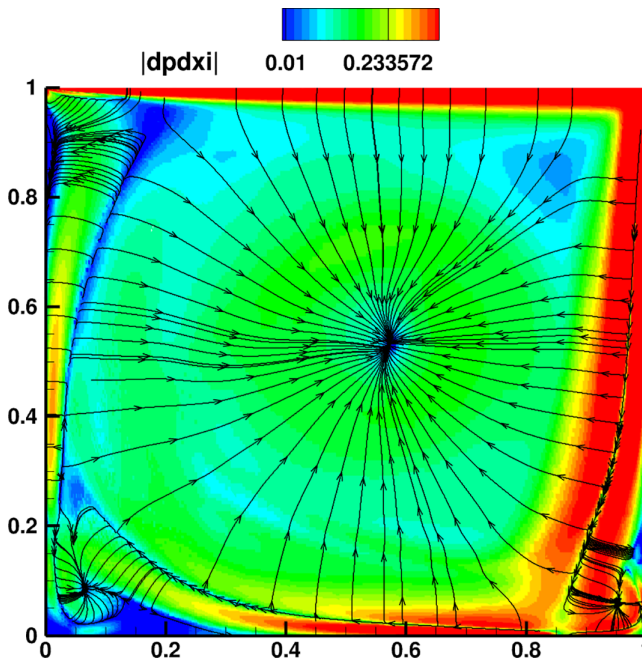FIG. 4. $\langle \vec{u} \times \vec{\omega} \rangle_y$ in the cavity in the steady state.

FIG. 5. Color: $|\langle \nabla P_s \rangle|$ in the cavity. The lines are tangential to the direction of $\langle \nabla P_s \rangle$.

except at the bottom where the separated sheet impinges on the bottom wall and contributes to an increased pressure on that boundary.

Figure 5 shows the direction and magnitude of $\langle \nabla P_s \rangle$, demonstrating Eq. (2b) and Figs. 1 and 2 for a simulated flow. Inside the vortices, the gradient points toward the center of rotation and are orthogonal to the streamlines seen in Fig. 3. The lines converge toward localized minima of stagnation pressure $\langle P_s \rangle$ which constitute the centers of the vortices.

V. CASE II - 6:1 PROLATE SPHEROID

The 6:1 prolate spheroid is a canonical geometry that is commonly used to study smooth three-dimensional separation. At the angle of attack, the boundary layer separates and forms a coherent, attached, counter-rotating vortex pair. A $20°$ incidence of the flow is chosen with a Reynolds number $Re_L = 4.2M$ where L is the length of the geometry. Numerical details are available in Plasseraud *et al.* [27], from which these results are taken. The flow is computed using wall-resolved Large Eddy Simulation on a 600M control volume overset grid tripped at $x/L = 0.2$. The statistics are averaged for one spheroid flow-through of time. In these conditions, the boundary layer separates along two separate longitudinal lines and two counter-rotating vortex pairs are formed, a primary pair and a smaller secondary pair underneath the primary separation sheet. A certain number of features make this flow particularly challenging to simulate and for vortex identification methods [27]:

The flow is characterized by several smooth 3D separations leading to several counter-rotating vortex pairs on the lee of the obstacle. Smooth separations are hard to resolve because they depend on the state of turbulence of the boundary layer; 3D separations are challenging to locate because they cannot be identified by the cancellation of the near-wall velocity or skin friction.

The vortex pairs are attached, which may be problematic for vortex identification since it is hard to isolate where the separated sheet ends and where the vortex begins. Isolating the separated sheet may be desirable for the purpose of analysis.
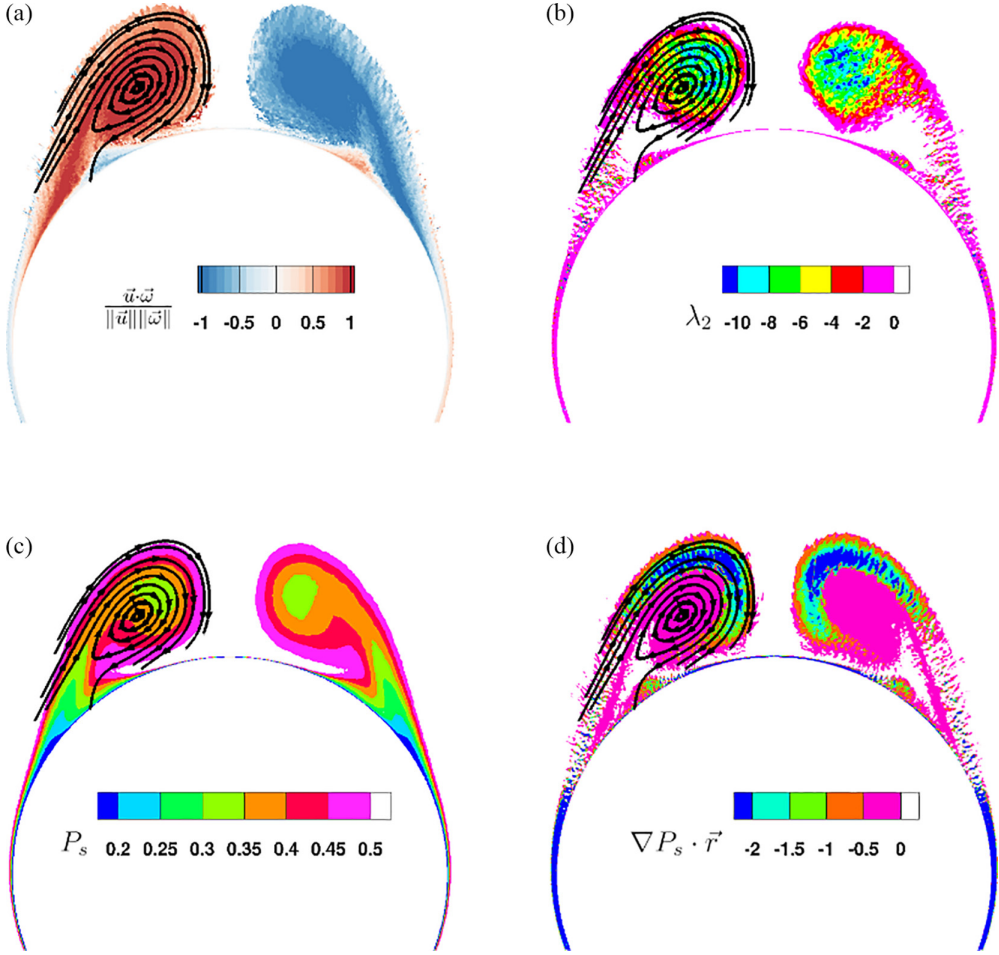
FIG. 6. Secondary streamlines and normalized helicity density (a) λ_2 (b) time-averaged stagnation pressure (b) $\langle \nabla P_s \cdot \vec{r} \rangle$ (d) in a transverse plane at $x/L = 0.772$, in the prolate spheroid flow at $20°$ incidence.

The vortices are strongly three-dimensional, which means that there is a net flux of momentum along their axis and that the streamlines are three-dimensional curves, complicating the vortex identification, especially for Lagrangian methods.

The multiple vortices and image vortices interact with each other to modify the velocity field. This implies that the center of each vortex has a nonzero velocity magnitude.

The surface of the spheroid is curved thus identification methods based on streamline curvature alone (i.e., Q and λ_2 method) may interpret the attached flow as a vortex.

The separation sheet and the primary vortex pairs have normalized helicity magnitudes that are close to unity (Beltrami flow), where the velocity vector and the vorticity vectors are almost colinear even though they have nonzero norms. This may challenge the proposed method that relies on Lamb surfaces, which could become undefined in Beltrami flows.

Figure 6(a) shows secondary streamlines and normalized helicity density on the lee of the prolate spheroid at $x/L = 0.772$, where x is the axial coordinate. The streamlines display the primary vortex pair as well as the separation sheet. The helicity density shows the primary vortex pair, the separated sheet as well as the small counter-rotating secondary vortex pair close to the wall. The helicity is very close to one in both the separation sheet and in the center part of the primary recirculation
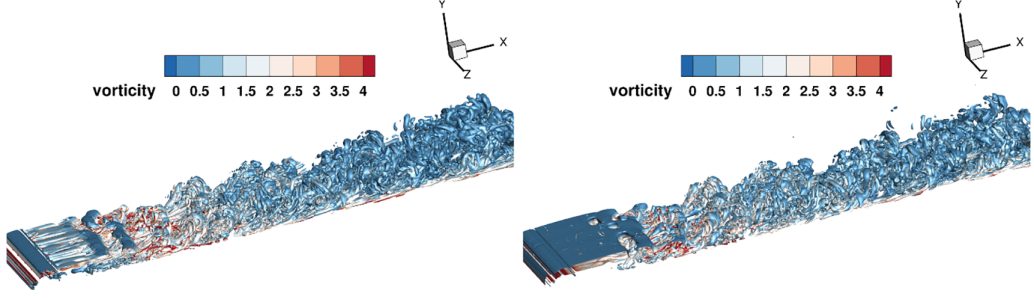
FIG. 7. $\lambda_2 = -0.01$ (left) and $\nabla P_s \cdot \vec{r} = -0.1$ isosurfaces (right) colored by instantaneous spanwise vorticity, in the tripped boundary layer case at $Re = 1000$.

region; while its absolute value is between 0.5 and 1 in the outer part of that area. In Fig. 6(b), $\langle \lambda_2 \rangle$ captures the general area around the vortex, however, the boundary does not align well with the streamlines and it does not represent the elliptical shape seen on the streamlines and in helicity. Furthermore, the center of the primary vortices cannot be reliably located as the minimum is too noisy. Similar values of $\langle \lambda_2 \rangle$ are seen between the attached boundary layer, the separation sheet and the entire secondary vortices, making it hard to discriminate between these three features. This lack of contrast comes from the difficulty the λ_2 method has in eliminating attached curved streamlines from detached ones as discussed above. Figure 6(c) shows the time-averaged stagnation pressure. The core is distinctly visible as a closed circular region of lower pressure. The separation is identifiable as a saddle in this transverse plane. The isolines on the outer part of the recirculation and the separation agree well with the streamlines although the predicted location of the core is offset from the minimum of secondary velocity, similarly to λ_2. This is due to the induced velocity from the other real and mirror vortices as discussed previously. In Fig. 6(d), $\langle \nabla P_s \cdot \vec{r} \rangle$ agrees even better with the secondary streamlines. The separation sheet and the inner part of the vortex where the helicity is unity, are distinctly visible as a negative, close to zero value. The separation sheet is thin and allows us to both identify the location of separation and the point of contact with the primary vortex. Surprisingly, another region is visible in the recirculation, which surrounds about half of the inner vortex and has a lower gradient of stagnation pressure. This pattern, along with the observations on the helicity, shows that the fluid from the separating boundary layer is first advected in the center of the vortex rather than at the periphery. The vorticity is then diffused from the core to the outer region that appears with a strong gradient of stagnation pressure. In addition, a secondary vortex pair is identifiable close to the wall and distinct from the turbulent boundary layer. The capacity of the proposed method to distinguish between the various layers of the vortex and clearly isolate the separation and small secondary vortices close to the wall is a unique and invaluable property for the study of complex flows.

The following two cases demonstrate the ability of the method to visualize complex unsteady turbulent flows.

VI. CASE III - TRIPPED BOUNDARY LAYER

The stagnation pressure method is first used for a flow over a flat plate with zero pressure gradient. The flow is tripped using a horizontal cylindrical wire of unit diameter. The Reynolds number based on trip height is 1000; the inflow is prescribed as a Blasius profile of boundary layer thickness $\delta_{99} = 1.5$. The flow is resolved using a wall-resolved Large Eddy Simulation. More details about the simulation and the results are provided in Plasseraud *et al.* [28], from which the results are taken. The challenge of vortex identification methods in this case, is to isolate vorticity inside vortices (vortical vorticity) from vorticity in the boundary layer (shearing) since the wake develops in a boundary layer. Figure 7 shows the $\lambda_2 = -0.01$ (left) and $\nabla P_s \cdot \vec{r} = -0.1$ isosurfaces
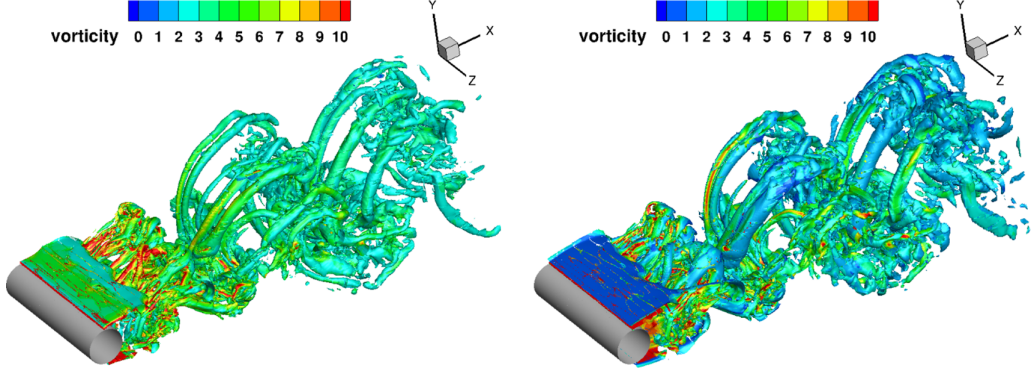
FIG. 8. Cylinder flow at $Re = 1000$: $\lambda_2 = -1$ isosurface (left) and $\nabla P_s \cdot \vec{r} = -0.6$ isosurface (right), colored by instantaneous vorticity magnitude.

in the region downstream of the trip. Both methods have very similar results, showing the complex development of hairpin vortices in the wake of the trip. The boundary layer upstream of the trip has a Blasius profile, which contains nonvortical vorticity. The proposed method successfully isolates the vortical vorticity from the shearing and does not show any surface from the upstream region. The two methods diverge slightly in the near wake of the trip, where the separation sheet is wavier with the λ_2 method compared to a flatter surface for the stagnation pressure method. This is due to the former method capturing more rotational motion of the streamwise instabilities while the latter is better at identifying separation with a longer radius of curvature.

VII. CASE IV - CYLINDER

The flow around an infinite cylinder for a Reynolds number based on a diameter of 1000 is calculated. A constant inflow of velocity U^∞ is prescribed, with a Neumann boundary as the outflow. The domain is four diameters in the span with 30M control volumes. Figure 8 shows the $\lambda_2 = -1$ isosurface (left) and the $\nabla P_s \cdot \vec{r} = -0.6$ isosurface (right), both colored by instantaneous vorticity magnitude. This regime is characterized by alternate periodic shedding of spanwise vortices at measured Strouhal number $St = fD/U^\infty \approx 0.196$ (where f is the frequency of shedding and D is the diameter of the cylinder) with smaller streamwise, elongated counter-rotating vortices connecting the primary ones. The proposed method is able to capture the unsteady flow in the wake of the cylinder even at a low Reynolds number. It also correctly shows the primary and secondary structures and gives similar results as λ_2. The stagnation pressure method successfully captures a large range of vortices sizes and topologies and successfully isolates the streamwise counter-rotating vortex pairs. Some differences are observed between the two methods: the shapes of the vortices are slightly different (visible with different values of vorticity). Similarly to the tripped flow problem (see Sec. III), the stagnation pressure method successfully isolates the vortical vorticity from shearing.

VIII. CASE V - JET IN A CROSS-FLOW

The proposed method is applied on the direct numerical simulation of the jet in a cross-flow case performed by Morse and Mahesh [29]. The jet-to-cross-flow velocity ratio is 2 and the Reynolds number based on jet velocity and nozzle diameter D is 2000. A triangular tab is placed on the upstream side of the nozzle. Numerical details and discussion of the results are available in Morse and Mahesh [29]. Figure 9 shows an isosurface of $\nabla P_s \cdot \vec{r}$. This jet flow is characterized by a large counter-rotating vortex pair that tilts in the direction of the cross-flow with increasing streamwise distance. This pair is accompanied by a series of smaller, unsteady spanwise vortices that are
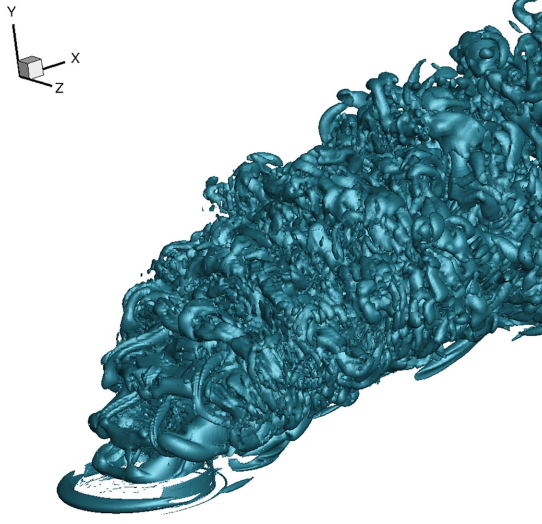
FIG. 9. Jet in cross-flow at $Re = 2000$ [29]: $\nabla P_s \cdot \vec{r} = -0.2$ isosurface.

periodically shed from the upstream part of the nozzle. Finally, tertiary structures referred to as lambda vortices connect the spanwise vortices. Figure 10 represents a transverse slice at $x = 6.7D$, showing the time-averaged stagnation pressure and Lamb contours in this plane. Both stagnation pressure isolines and Lamb contours agree well. The counter-rotating vortex pair (CRVP) is visible as a doublet of closed stagnation pressure isoline, which is visibly similar to the closed Lamb contours. The secondary, horseshoe vortex is visible on each side of the CRVP while the lambda vortices are visible on top. Figure 11 shows the time-averaged stagnation pressure in transverse planes from $x = 5D$ to $x = 15D$ by 2.5D step. The counter-rotating vortex pair is clearly visible as two closed areas of stagnation pressure. The size of the two vortices remains roughly constant with
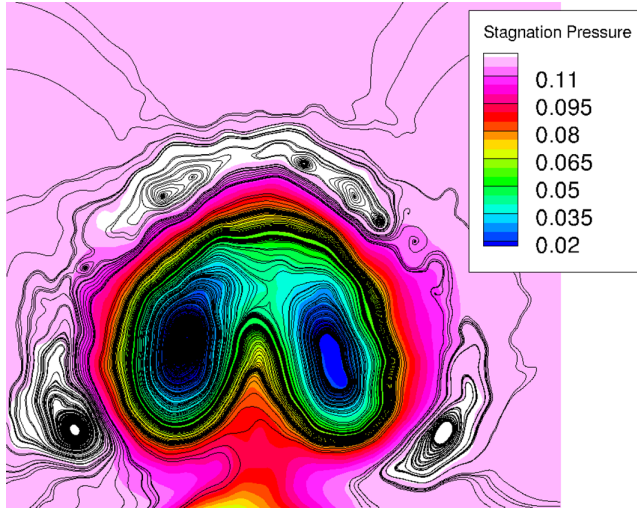

FIG. 10. Transverse view of the jet in cross-flow at $Re = 2000$ and at 6.7 nozzle diameter downstream of the nozzle center line: the color represents the time-averaged stagnation pressure, and the lines are time-averaged Lamb lines.
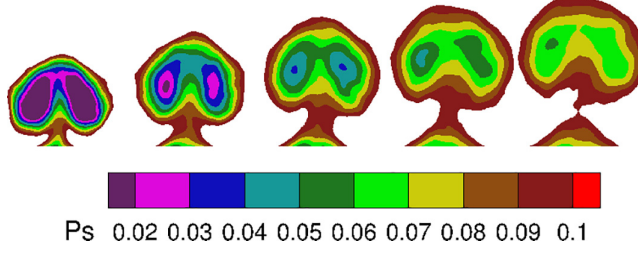
FIG. 11. Transverse view of the jet in cross-flow at $Re = 2000$ from five to 15 nozzle diameters downstream: the color represents the time-averaged stagnation pressure.

the streamwise coordinate although their strength diminishes as indicated by increasing values of stagnation pressure.

IX. CONCLUSION

A new vortex identification methodology is proposed for incompressible flows, which uses closed Lamb surfaces, approximated by isosurfaces of stagnation pressure as a vortex boundary. More specifically, a vortex is contained in the following region:

(1) Vortex core: $P_s = P'/\rho + 1/2 u_i u_i \leqslant P_s^0$ where P_s^0 is the value of a closed isoline.

(2) Outer vortex region: $(\vec{u} \times \vec{\omega}) \cdot \vec{r} < 0$ approximated as $\nabla P_s \cdot \vec{r} < 0$ with $\|\nabla P_s\| > 0$. $\vec{r}$ is a vector that points towards the local curvature of the flow and can be calculated by normalization of the vector $\partial u_i / \partial x_j \cdot u_j$.

(3) Vortex center: minimum of P_s and $\|\nabla P_s\|$.

The method is robust, fast to converge, trivial to use, and can be applied to both steady and unsteady flows. The theoretical basis originates from Crocco's theorem, which guarantees that in the inviscid limit, streamlines are tangential to stagnation pressure isosurfaces while the norm of the stagnation pressure gradient is minimal at vortex centers. Despite the assumption of inviscid flow, the method has demonstrated excellent identification abilities even at moderate Reynolds numbers. The method can be used to help estimate vortex loads by using the relation between $\vec{u} \times \vec{\omega}$ and the isoline of stagnation pressure. For experimental purposes where the pressure field is not readily available, vortices can instead be visualized with isosurfaces of $\nabla \frac{1}{2} u_i u_i \cdot \vec{r} < 0$, which approximates the stagnation pressure criterion when the pressure gradient is negligible compared to the gradient of kinetic energy.

[1] H. J. Lugt, The dilemma of defining a vortex, in *Recent Developments in Theoretical and Experimental Fluid Mechanics: Compressible and Incompressible Flows* (Springer, Berlin, Heidelberg, 1979), pp. 309–321.

[2] S. K. Robinson, Coherent motions in the turbulent boundary layer, Annu. Rev. Fluid Mech. **23**, 601 (1991).

[3] V. Holmén, Methods for vortex identification, Master's thesis, Lund University, Lund, Sweden, 2012.

[4] B. Epps, Review of vortex identification methods, in *Proceedings of the 55th AIAA Aerospace Sciences Meeting* (AIAA, Grapevine, Texas, 2017), p. 0989.

[5] G. Haller, An objective definition of a vortex, J. Fluid Mech. **525**, 1 (2005).

[6] J. Li and P. M. Carrica, A simple approach for vortex core visualization, J. Fluids Eng. **142**, 051504 (2020).

[7] P. G. Saffman, *Vortex Dynamics* (Cambridge University Press, Cambridge, UK, 1995).

[8] P. Comte, J. Silvestrini, and P. Bégou, Streamwise vortices in large-eddy simulations of mixing layers, Eur. J. Mech.-B/Fluids **17**, 615 (1998).

[9] J. C. Hunt, A. A. Wray, and P. Moin, Eddies, streams, and convergence zones in turbulent flows, *Studying Turbulence Using Numerical Simulation Databases, 2. Proceedings of the 1988 Summer Program* (Center for Turbulence Research, Stanford, California, USA, 1988).

[10] Y. Dubief and F. Delcayre, On coherent-vortex identification in turbulence, J. Turbul. **1**, N11 (2000).

[11] J. Jeong and F. Hussain, On the identification of a vortex, J. Fluid Mech. **285**, 69 (1995).

[12] S. Robinson, S. J. Kline, and P. Spalart, A review of quasi-coherent structures in a numerically simulated turbulent boundary layer, in *Quasi-Coherent Structures in the Turbulent Boundary Layer, part 2. Verification and New Inform. from a Numerically Simulated Flat-Plate Layer at Memorial Intern. Seminar on Near-Wall Turbulence, NASA-TM-102191* (NASA Ames, Dubrovnik, Yugoslavia, 1989).

[13] G. Haller, A. Hadjighasem, M. Farazmand, and F. Huhn, Defining coherent vortices objectively from the vorticity, J. Fluid Mech. **795**, 136 (2016).

[14] M. M. Neamtu-Halic, D. Krug, G. Haller, and M. Holzner, Lagrangian coherent structures and entrainment near the turbulent/non-turbulent interface of a gravity current, J. Fluid Mech. **877**, 824 (2019).

[15] C. Truesdell, *The Kinematics of Vorticity* (Indiana University Press, Bloomington, Indiana, 1954).

[16] Y. Levy, D. Degani, and A. Seginer, Graphical visualization of vortical flows by means of helicity, AIAA J. **28**, 1347 (1990).

[17] A. F. Hussain, Coherent structures and turbulence, J. Fluid Mech. **173**, 303 (1986).

[18] M. Howe, On the force and moment on a body in an incompressible fluid, with application to rigid bodies and bubbles at high and low reynolds numbers, Q. J. Mech. Appl. Math. **48**, 401 (1995).

[19] M. Germano, U. Piomelli, P. Moin, and W. H. Cabot, A dynamic subgrid–scale eddy viscosity model, Phys. Fluids A **3**, 1760 (1991).

[20] D. K. Lilly, A proposed modification of the Germano subgrid–scale closure model, Phys. Fluids A **4**, 633 (1992).

[21] A. Verma and K. Mahesh, A Lagrangian subgrid-scale model with dynamic estimation of Lagrangian time scale for large eddy simulation of complex flows, Phys. Fluids (1994-present) **24**, 085101 (2012).

[22] T. B. Kroll and K. Mahesh, Large-eddy simulation of a ducted propeller in crashback, Flow **2**, E4 (2022).

[23] P. Kumar and K. Mahesh, Large eddy simulation of flow over an axisymmetric body of revolution, J. Fluid Mech. **853**, 537 (2017).

[24] N. Morse and K. Mahesh, Large-eddy simulation and streamline coordinate analysis of flow over an axisymmetric hull, J. Fluid Mech. **926**, A18 (2021).

[25] K. Mahesh, G. Constantinescu, and P. Moin, A numerical method for large-eddy simulation in complex geometries, J. Comput. Phys. **197**, 215 (2004).

[26] W. J. Horne and K. Mahesh, A massively-parallel, unstructured overset method to simulate moving bodies in turbulent flows, J. Comput. Phys. **397**, 108790 (2019).

[27] M. Plasseraud, P. Kumar, and K. Mahesh, Large-eddy simulation of tripping effects on the flow over a 6:1 prolate spheroid at angle of attack, J. Fluid Mech. **960**, A3 (2023).

[28] M. Plasseraud, P. Kumar, R. Ma, and K. Mahesh, Simulation of flow over an inclined spheroid at high reynolds number: Tripping effects, in *Proceedings of the 34th Symposium on Naval Hydrodynamics* (Symposium on Naval Hydrodynamics, Washington, DC, 2022).

[29] N. Morse and K. Mahesh, Effect of tabs on the shear layer dynamics of a jet in cross-flow, J. Fluid Mech. **958**, A6 (2023).